Journal of Materials Chemistry A

ROYAL SOCIETY OF CHEMISTRY

PAPER

View Article Online
View Journal

Cite this: DOI: 10.1039/d5ta08108d

Oxygen vacancy-rich In_2O_3-ZrO_2 catalysts synthesized *via* DBD plasma for enhanced CO_2-to-CO conversion

Sai Li,*[a] Yuhang Wang,[a] Kui Zhang,[b] Haiyan Zhu,[c] Shaobo Jia,[c] Dongyuan Yang,[a] Peng Ren,[d] Zekai Ma,[a] Shuoshuo Wang,[a] Haixia Wu,[a] Yameng Ma,[a] Qi Chen,[a] Jiahao Zhouhuang,[a] Qiuliang Yu,[g] Lihui Zeng,[h] Rui Tan,[e] Zhiming Feng*[f] and Qing Feng*[d]

The efficient utilization of CO_2 as a carbon feedstock is vital for achieving carbon neutrality while enabling sustainable production of C_1 chemicals. Plasma-assisted catalytic conversion has emerged as a promising strategy under mild conditions, yet its progress is limited by the lack of highly active and plasma-tolerant catalysts. In this work, an In_2O_3-ZrO_2 composite catalyst with high catalytic activity, excellent thermal stability and long service life was successfully prepared by combining the chemical precipitation method with plasma technology. The In-Zr (1 : 1) catalyst exhibited the best performance, reaching a CO_2 conversion of 26.3% and CO selectivity above 90% at an SIE of 104 kJ L^{-1}. Compared with pure In_2O_3, the composite showed markedly improved thermal stability, sustaining continuous operation for 450 min, three times longer than In_2O_3. Plasma modification induced a higher concentration of oxygen vacancies (1.69×10^{13} spins per g), increased surface area (56.7 m^2 g^{-1}), and a narrowed bandgap (2.49 eV), which synergistically enhanced catalytic activity. Mechanistic studies and DFT calculations further revealed that the strong plasma-catalyst interaction facilitates CO_2 activation pathways. This study demonstrates not only the durability of In-Zr composites but also highlights plasma modification as an effective strategy to design next-generation catalysts for plasma-assisted CO_2 utilization. Meanwhile, the In-Zr catalyst successfully developed in this study, with its outstanding performance, stability and durability, is a highly promising candidate material for high-temperature industrial catalytic processes.

Received 4th October 2025
Accepted 5th January 2026

DOI: 10.1039/d5ta08108d

rsc.li/materials-a

1. Introduction

In recent years, the persistent rise in carbon dioxide (CO_2) emissions intensified concerns over global warming and climate risk, posing a major challenge to sustainable development.[1–5] Meanwhile, the global transition from fossil-fuel-based systems to low-carbon and hydrogen-enabled energy technologies is accelerating.[6–8] Therefore, converting CO_2 into high-value products, such as CO, CH_4, and CH_3OH,[9] *via* carbon capture and utilization (CCU) is regarded as one of the most effective scientific strategies.[10–13] Carbon monoxide (CO) possesses significant commercial value as a C_1 resource, serving as a precursor to produce various value-added chemicals.[10,14] Consequently, the direct conversion of CO_2 into CO and O_2 constitutes a significant industrial process.[15–17]

$$CO_2 = CO + 1/2O_2,\ \Delta H = 283\ \text{kJ mol}^{-1} \quad (1)$$

There are several methods for CO_2 conversion: pyrolysis, electrocatalysis, photocatalysis, and plasma catalysis. Nonetheless, due to the dissociation energy of C=O being 5.5 eV, the pyrolysis process requires elevated temperatures approaching 2000 K to facilitate the breakdown of CO_2. The catalysts employed in electrocatalytic and photocatalytic processes are often precious metal catalysts, which are relatively expensive. Conversely, non-thermal plasma technology (NTP) produces high-energy electrons ranging from 1 to 10 eV at ambient temperature and pressure,[18–20] which can cleave the C=O bond, thereby facilitating the decomposition and conversion of CO_2. Thus, NTP is considered a viable alternative to conventional conversion methods. Common plasma generation methods include glow discharge, microwave discharge, and dielectric

[a]School of Chemistry and Chemical Engineering, Xi'an University of Science and Technology, Xi'an, 710054, China. E-mail: saili@xust.edu.cn
[b]School of Engineering, Newcastle University, Newcastle Upon Tyne NE1 7RU, UK
[c]Shaanxi Key Laboratory for Theoretical Physics Frontiers, Institute of Modern Physics, Northwest University, Xi'an, Shaanxi 710069, China
[d]Xi'an Tai Jin Xin Neng Technology Co., Ltd, Xi'an, 710201, China. E-mail: fengqing0715@126.com
[e]Department of Chemical Engineering, Swansea University, Swansea, SA1 8EN, UK
[f]Department of Chemical Engineering, University of Manchester, Manchester, M13 9PL, UK. E-mail: zhiming.feng@manchester.ac.uk
[g]Shaanxi Anchuang Electronic Technology Co., Ltd, Xi'an, 710201, China
[h]Kaili Catalyst New Materials Co., Ltd, Xi'an, 710201, China

barrier discharge (DBD).[21] Among them, DBD is more appropriate for CO_2 conversion owing to its benefits of stable discharge, homogeneous gas distribution, and effective gas tightness.[22–25]

The NTP technique for CO_2 processing offers advantages such as (1) operation at ambient temperature and pressure, (2) reduced energy input requirements, and (3) enhanced CO selectivity. Nevertheless, the limited utilization of high-energy electrons produced by NTP prevents a single plasma from attaining high CO_2 conversion efficiency. Consequently, the integration of plasma technology with catalysts to collaboratively facilitate the breakdown of CO_2 is the primary research focus in this domain.[26] In 2020,[27] Ray *et al.* introduced a g-C_3N_4 – based catalyst into a DBD system and demonstrated that 5% ZnO + g-C_3N_4 enhanced the catalytic conversion of acidic gases, such as CO_2, owing to the abundance of alkaline sites. In 2023,[28] Rao *et al.* investigated the synergistic catalytic effects of several alkali metal oxides with DBD, revealing a trend of SrO > Al_2O_3 > MgO > CaO. In 2024,[29] Hadi *et al.* confirmed that oxygen vacancies in metal oxides enhanced the catalytic breakdown of CO_2.

Cubic-phase indium oxide (c-In_2O_3) is notable among many metal oxides that tend to produce oxygen vacancies, owing to its stable thermodynamic configuration and superior catalytic performance.[30,31] We previously synthesized In_2O_3 nanocatalysts with elevated oxygen vacancies using chemical precipitation coupled with DBD technology and confirmed their efficacy in synergistically enhancing the catalytic conversion of CO_2 when used with DBD.[32,33] In_2O_3 has remarkable catalytic activity at lower temperatures (225 °C), but at elevated temperatures, it experiences a significant decrease in activity, resulting in catalyst deactivation.

To address the issues of short lifespan and thermal deactivation of In_2O_3 catalysts, our research team selected ZrO_2 as a second component owing to its excellent thermal stability and catalytic potential, based on preliminary screening experiments. In this study, In_2O_3-ZrO_2 composite catalysts with different indium–zirconium molar ratios were successfully prepared by combining chemical precipitation and DBD technology and placed in a DBD reactor to explore the effects of synergistic interactions between catalysts and DBD plasma on the catalytic conversion of CO_2. It is important to promote the application of plasma catalysis technology in CO_2 conversion. This work aims to promote the application of plasma-catalysis technology in CO_2 conversion. The catalytic performances of In_2O_3, ZrO_2 and In_2O_3-ZrO_2 catalysts with different indium–zirconium ratios were compared in a DBD reactor. In addition, the composite catalysts were analyzed to gain insight into improving the reaction mechanism for the catalytic conversion of CO_2 in the DBD reactor and the possible reasons for its high lifetime.

2. Experimental

2.1 Plasma reactor setup

Fig. 1 illustrates the interior configuration of the experimental apparatus and DBD reactor. The reaction gas utilized was high-purity CO_2 (Shanxi Lizhe Gas Corporation, purity: 99.99%), with the flow rate regulated between 10–80 mL min^{-1} using a pressure regulator valve and a mass flow meter (ACU10FD-LC, produced by Beijing AccuFlow Technology Co., Ltd). After flow regulation, the gas was introduced at one end of the DBD reactor, traversed the plasma region to undergo the reaction, and subsequently, the reaction products were collected at the opposite end. The gaseous products of the reaction were analyzed using a GC9790 II gas chromatograph equipped with a thermal conductivity detector (TCD) to determine their composition after reaction. The experiment utilized a high-voltage AC power supply as the power source. The detailed setup is shown in Fig. 1a.

Fig. 1b illustrates the internal structure of the DBD reactor. The primary structure of the DBD reactor comprises a quartz tube with an internal diameter of 15 mm. A stainless-steel rod, measuring 13 mm in diameter and 150 mm in length, is positioned along the axis within the quartz tube as the inner electrode. A 120-mm-long stainless-steel mesh was positioned around the outer surface of the quartz tube to serve as the outer electrode. The reactor's discharge gap measured 1 mm, while the discharge length was 120 mm. The catalyst was introduced into the DBD reactor *via* the incorporated powder catalyst (IPC) approach. The plasma power signal was measured using a TM10 oscilloscope (Tecman Electronic Instrument Holdings Limited).[34]

2.2 Catalyst preparation

The catalysts were synthesized using a chemical precipitation process integrated with DBD plasma technology. Using the catalyst with an In_2O_3-ZrO_2 molar ratio of 1 : 1 (designated as In-Zr (1 : 1)) as a case study: initially, 1.86 g of indium nitrate and 1.07 g of zirconium nitrate were dissolved in 50 mL of deionized water to create the precursor solution, followed by the dissolution of sodium carbonate in deionized water to prepare a sodium carbonate solution at a concentration of 0.2 mol L^{-1}. The catalyst was synthesized using chemical impregnation while stirring at 80 °C and 800 rpm, using a syringe pump to maintain a flow rate of 120 mL min^{-1}. Subsequently, the sodium carbonate solution was gradually added to the precursor solution *via* a syringe pump at 120 mL min^{-1} under continuous stirring (80 °C, 800 rpm) until the pH reached 10. Following a three-hour aging period at 80 °C, the suspension was filtered, rinsed with hot deionized water, and then dried at 80 °C for 12 hours, followed by calcination in a muffle furnace (heating rate of 5 °C min^{-1}, calcination temperature of 450 °C, duration of 3 hours). The resultant powder samples were positioned in a DBD reactor and treated in batches at 60 W for 20 minutes, ultimately yielding a light yellow powdered In-Zr (1 : 1) catalyst. The specific raw material dosages and reaction parameters of other catalysts prepared by the chemical precipitation method are shown in Table 1.

A mechanical grinding method was adopted to prepare the physically mixed composite catalyst. The experimental procedures are as follows: 2.77 g of In_2O_3 sample and 1.23 g of ZrO_2 sample were dried and uniformly mixed, followed by grinding

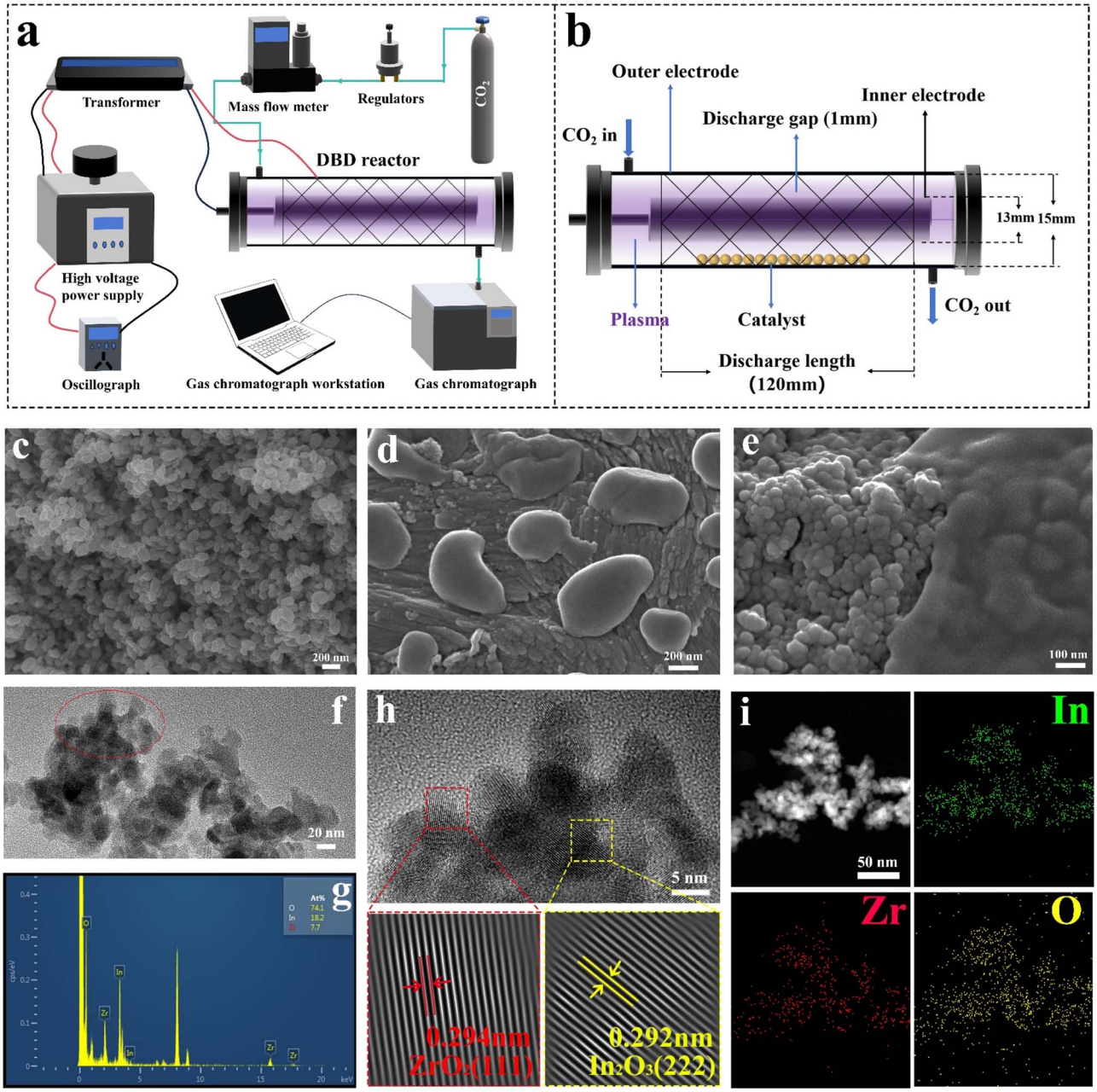

Fig. 1 Schematic of the experimental setup and the details of a cylindrical DBD plasma reactor: (a) schematic of the experimental setup; (b) details of the cylindrical DBD plasma reactor. SEM image of (c) In_2O_3, (d) ZrO_2, and (e) In-Zr (1 : 1); (f) TEM image of In-Zr (1 : 1), (g) EDS analysis of In-Zr (1 : 1), (h) HRTEM image of In-Zr (1 : 1), (i) HAADF-STEM image and elemental mapping images of In-Zr (1 : 1).

Table 1 Catalyst preparation parameters

Catalyst type	Dosage of $In(NO_3)_3$	Dosage of $Zr(NO_3)_4$	Stirring rate	Calcination conditions
In_2O_3	3.00 g	0 g	800 rpm	450–5 °C min^{-1}
In-Zr (7 : 3)	2.61 g	0.64 g	800 rpm	450–5 °C min^{-1}
In-Zr (1 : 1)	1.86 g	1.07 g	800 rpm	450–5 °C min^{-1}
In-Zr (3 : 7)	1.12 g	1.50 g	800 rpm	450–5 °C min^{-1}
ZrO_2	0 g	3.00 g	800 rpm	450–5 °C min^{-1}

in a mortar for 10 minutes to ensure sufficient mixing. Finally, the target physically mixed composite catalyst was obtained.

2.3 Chromatographic analysis and parameter definition

The CO_2 conversion rate, CO yield, and CO selectivity were defined as

$$CO_2\ \text{conversion rate}\ (\%) = \left[\frac{CO_2\ \text{in} - CO_2\ \text{out}}{CO_2\ \text{in}}\right] \times 100 \quad (2)$$

$$\text{CO yield}\ (\%) = \left[\frac{\text{CO out}}{CO_2\ \text{in}}\right] \times 100 \quad (3)$$

$$\text{CO selectivity}\ (\%) = \left[\frac{\text{CO out}}{CO_2\ \text{in} - CO_2\ \text{out}}\right] \times 100 \quad (4)$$

where CO_2 in, CO_2 out, and CO out are the molar flow rate of input CO_2 (mol min^{-1}), and output of CO_2 (mol min^{-1}) and CO (mol min^{-1}), respectively.

The specific input energy (SIE) is defined as.

$$\text{SIE}\ \left(\text{kJ L}^{-1}\right) = \left[\frac{\text{input power (W)} \times 60}{F_{CO_2\ \text{in}}}\right] \quad (5)$$

where $F_{CO_2\ \text{in}}$ is the flow rate of CO_2 (mL min^{-1}).

The energy efficacy of the reaction is defined as.

$$\eta\ (\%) = \left[\frac{CO_2\ \text{conversion} \times \Delta H\ \left(\text{kJ mol}^{-1}\right)}{22.4 \times \text{SIE}}\right] \quad (6)$$

The residence time of CO_2 in the DBD device was determined by the following equation.

$$\text{Residence time (s)} = \left[\frac{V}{F_{CO_2\ \text{in}}}\right] \times 60 \quad (7)$$

where V represents the volume of the DBD plasma zone, which is 5.3 mL, and F represents the various inlet flow rates.

2.4 Catalyst characterization

The various c-catalyst samples were individually analyzed using X-ray diffraction (MiniFlex 600), and spectra were produced within the range of $2\theta = 0°$–$90°$. The microstructures of various catalysts were examined with a Hitachi SU8230 field emission scanning electron microscope and an FEI Tecnai F20 transmission electron microscope, while the elemental compositions of the In-Zr (1 : 1) catalysts were analyzed using an X-Twin energy-dispersive X-ray spectrometer (EDS). The surface chemical compositions and oxidation states of the various catalysts were ascertained using X-ray photoelectron spectroscopy (Thermofisher ESCALAB Xi+). The quantity of bulk oxygen vacancies in the samples was assessed using electron paramagnetic resonance (EPR) spectroscopy (Bruker A300 Germany). A Shimadzu 3600-Plus UV-Vis spectrometer was employed to acquire diffuse reflectance UV-Vis spectra spanning 200–800 nm, and the bandgap energies were determined using the Tauc plot technique. Ultimately, CO_2 adsorption and desorption studies were conducted utilizing a kinetic gas adsorption analyzer (Conta Autosorb-iQ) at 273 K, with CO_2 as the adsorbate gas. All samples were degassed under vacuum at 120 °C for 7 hours prior to analysis. The surface area of each catalyst was determined using the BET (Brunauer–Emmett–Teller) technique, while the pore volume and pore size of each catalyst were measured from the BJH (Barrett–Joyner–Halenda) desorption curve.

The specific parameters of the Density Functional Theory (DFT) simulation calculations are as follows:

Computational software and procedures: all first-principles calculations were performed using the Vienna *Ab initio* Simulation Package (VASP). Modelling and visualisation were conducted using Materials Studio and VESTA software.

Exchange-correlation functional: The Perdew–Burke–Ernzerhof (PBE) functional under the generalized gradient approximation (GGA) was employed.

Dispersion correction: to accurately describe intermolecular weak interactions, the DFT-D3 method was employed for dispersion correction.

Planar wave cutoff energy: set to 520 eV.

Electronic self-consistency iterations: energy convergence criterion set to EDIFF = 10^{-5} eV.

Atomic geometry optimisation: force convergence criterion on each atom set to EDIFFG = 0.02 × eV $Å^{-1}$.

3. Results and discussion

3.1 Microscopic morphology of the catalyst

The surface morphology of In_2O_3, ZrO_2, and In-Zr (1 : 1) was characterized using scanning electron microscopy (SEM), as seen in Fig. 1c–e. Fig. 1c and d show the SEM images of In_2O_3 and ZrO_2, respectively. In_2O_3 exists as nanoparticles with an average size of around 100 nm, while ZrO_2 exhibits a distinct morphology characterized as 'amorphous,' with particle sizes ranging from 200 to 400 nm. The particle size ranges from 200 to 400 nanometers. Fig. 1e illustrates the surface morphology of In-Zr (1 : 1) composite catalysts, revealing the nanoparticle morphology of In_2O_3 alongside the droplet-like structure of ZrO_2. A distinct interface between the various morphologies is evident, signifying that the structure is heterogeneous, comprising In_2O_3 and ZrO_2. The presence of multiple heterogeneous interfaces increases the exposure of active sites, thereby enhancing catalytic activity.

The catalysts' morphological characteristics were examined and analyzed by transmission electron microscopy. Fig. 1f presents the TEM image of the In-Zr (1 : 1) catalyst, whereas Fig. 1h displays the HRTEM image corresponding to its designated location. The assessment of the catalysts through Fourier and inverse Fourier transformations (Fig. S1), along with lattice spacing measurements, indicates that the In-Zr (1 : 1) catalyst displays two lattice fringes corresponding to the (111) crystallographic plane of ZrO_2 and the (222) crystallographic plane of In_2O_3, thereby reaffirming the heterogeneous structure of the In-Zr (1 : 1) catalyst. Meanwhile, we have performed SAED analysis of the composite sample, with the results presented in Fig. S1. It can be seen that the diffraction pattern consists of diffraction rings rather than diffraction spots, indicating that this region has a polycrystalline structure. Additionally, through

the analysis of these diffraction rings, they can be indexed to different crystal planes of In_2O_3 and ZrO_2, which further confirms the component composition of the composite catalyst.

Fig. 1i presents the HAADF-STEM and elemental mapping images of the catalysts, accompanied by energy dispersive X-ray spectroscopy (EDS) and elemental analysis (Fig. 1g and S2). Fig. 1e illustrates that, among the three constituents In, Zr, and O in the catalyst, the O element predominates, while the molar ratio of In to Zr is approximately 2 : 1. This observation aligns with the design of the composite catalyst, In-Zr (1 : 1), where the molar ratio of In_2O_3 to ZrO_2 is also 1 : 1. The elemental mapping image (Fig. 1g) reveals a homogeneous distribution of the elements In, Zr, and O throughout the catalyst. This confirms that the In-Zr (1 : 1) catalyst consists of a heterogeneous composition, with ZrO_2 and In_2O_3 interwoven. This heterogeneous structure enhances catalytic activity, while the interaction of the dioxide phases improves the overall performance of the catalyst through synergistic effects.

We also conducted SEM and TEM characterizations on the In-Zr (1 : 1) composite catalyst after DBD treatment, and the detailed results are presented in Fig. S3. A comparison of the SEM images before and after treatment reveals that the catalyst's overall morphology, particle size, and distribution remained consistent. Low-magnification TEM images further confirm that DBD treatment did not cause obvious sintering, fragmentation, or agglomeration of the particles. To investigate potential effects on the crystal structure, we conducted HRTEM analysis. It can be observed that the clear lattice fringes in the catalyst were completely retained after treatment. These data strongly indicate that the DBD plasma treatment we employed is a mild and highly selective surface modification technique. This technique enables precise regulation of the catalyst's surface properties without altering its bulk morphology or crystal structure.

3.2 Catalytic activity evaluation

To validate the catalytic conversion of CO_2 by various catalysts in the DBD reactor, 0.2 g of each catalyst was introduced into the DBD reactor using the IPC method. The CO_2 inlet flow rate was maintained at 20 mL min^{-1}, while the specific energy input (SIE) of the system was regulated by modulating the input power. The test outcomes are illustrated in Fig. 2. Fig. 2a and b illustrate that an increase in the specific energy input of the DBD system resulted in a substantial enhancement in CO_2 conversion and CO production. This occurs because, at elevated SIE, the plasma generates more energetic electrons, thereby increasing the collision likelihood between CO_2 and these electrons, ultimately improving CO_2 conversion.[35] The catalyst-filled DBD exhibits a substantial enhancement in CO_2 conversion and CO yield relative to the catalyst-free DBD. This results from the synergistic interaction between the catalyst and plasma discharge in CO_2 conversion.[19,36] The total CO_2 conversion efficacy follows the sequence: In_2O_3 > In-Zr (7 : 3) > In-Zr (1 : 1) > In-Zr (3 : 7) > ZrO_2. From this, In_2O_3 demonstrates a greater contribution to CO_2 conversion than ZrO_2. Fig. 2d illustrates that the maximum CO yield is achieved in the DBD system containing In-Zr in a 1 : 1 ratio. In conjunction with the CO selectivity illustrated in Fig. 2c, it is evident that the CO selectivity of the DBD reactors diminished to varied extents following the introduction of the catalysts, although the CO selectivity of the In-Zr (1 : 1) synergistic DBD consistently remained elevated (>90%). This explains the high CO yield observed with the In-Zr (1 : 1) DBD system at increased SIE. The In-Zr (1 : 1) catalyst therefore selectively promotes the conversion of CO_2 to CO within the DBD reactor.

Fig. 2d illustrates the comparative energy efficiency of several catalysts over different SIEs. The energy efficiency of DBD systems containing catalysts surpasses those of the empty DBDs, indicating that the presence of catalysts enhances the utilization of energy for CO_2 conversion rather than for heat dissipation.

The catalyst's stability is similarly crucial in practical applications. In the operation of DBD, the gas temperature within the system rises with increasing input power[37] (Fig. S4), and excessive temperatures might adversely influence the catalytic activity of the catalyst. To assess the thermal stability of several catalysts, 0.2 g of each catalyst was introduced into the DBD reactor using the IPC technique and evaluated at an input power of 80 W (SIE = 237 kJ L^{-1}, T = 251.8 °C). The findings are presented in Fig. 2e. During the early phase of the reaction, the CO_2 conversion in all reactors progressively rose over time, indicating that the catalyst is undergoing activation. At 50 minutes, the CO_2 conversion in the DBD reactor containing In_2O_3 and In-Zr (7 : 3) began to decrease gradually, ultimately stabilizing at approximately 16%, which is lower than that of the catalyst-free DBD. In contrast, the CO_2 conversion in the DBD reactor filled with In-Zr (1 : 1), In-Zr (3 : 7), and ZrO_2 catalysts continued to rise, eventually stabilizing at a level exceeding that of the catalyst-free DBD. The likely explanation for this behaviour is that ZrO_2 possesses significant thermal stability and its physicochemical properties remain stable at elevated temperatures, while the incorporation of ZrO_2 helps to preserve the catalytic activity of the catalysts under high-temperature conditions.

To investigate the service life of the composite catalyst, 0.2 g of In_2O_3 catalyst, ZrO_2 catalyst and In-Zr (1 : 1) catalyst, identified as the most effective among the composite catalysts, was introduced into a DBD reactor *via* the IPC method. The service life of the catalyst was measured under the condition of SIE = 104 kJ L^{-1}, where the system energy efficiency reaches its maximum. The results are shown in Fig. 2f. During the initial 0–80 minutes, the In_2O_3 catalyst undergoes an activation phase, during which the conversion of CO_2 progressively rises over time. During the 80–180 minute interval, the In_2O_3 catalyst remains in the stabilization phase, exhibiting negligible variation in its CO_2 conversion rate. After 180 minutes, the CO_2 conversion of In_2O_3 starts to decline and ultimately drops below that of the empty-loaded DBD. After activation, the ZrO_2 catalyst can also maintain a high CO_2 conversion rate. Although slightly lower than that of the In-Zr (1 : 1) composite catalyst, no obvious downward trend is observed, demonstrating excellent stability. In comparison, the activation duration of the In-Zr (1 : 1) catalyst significantly exceeds that of the pure In_2O_3 catalyst, with the

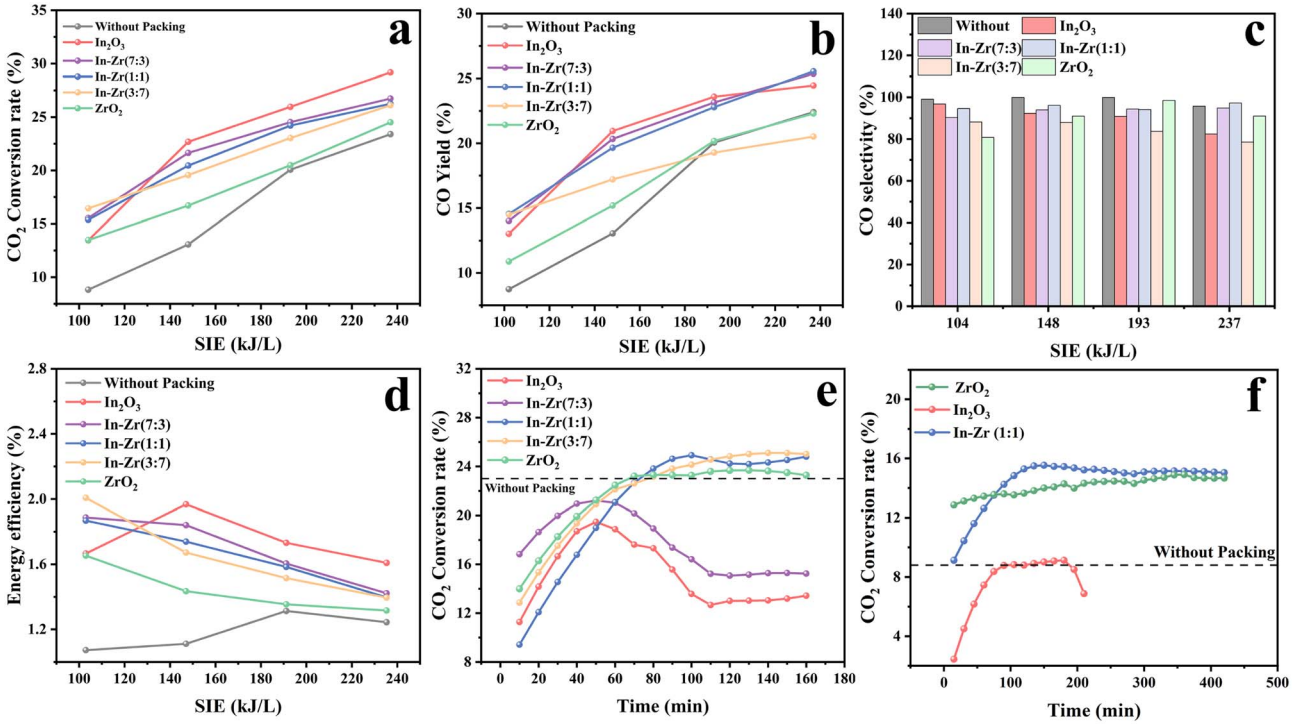

Fig. 2 The impact of SIE on (a) CO_2 conversion rate, (b) CO yield, (c) CO selectivity, and (d) energy efficiency of different packing materials; (e) thermal stability of different packing materials; (f) comparison of the lifetimes of In_2O_3 and In-Zr (1 : 1) under the optimal SIE.

former exhibiting an activation period of 0–150 minutes and consistently achieving superior CO_2 conversion rates during this timeframe. During the 150 to 450 minute interval, the In-Zr (1 : 1) catalyst exhibited stability, with CO_2 conversion remaining constant across time and no observable deactivation phase. This signifies that the catalyst's lifespan was significantly enhanced with the incorporation of ZrO_2.

Based on these findings, it was determined that the In-Zr (1 : 1) catalyst exhibited not only elevated CO_2 conversion and CO yield but also the capability to selectively break down CO_2 into CO, with superior thermal stability and longevity compared to the pure In_2O_3 catalyst. Consequently, the ensuing composite catalysts were investigated utilizing In-Zr (1 : 1) catalysts.

3.3 The effect of SIE and residence time

In order to investigate the effect of In-Zr (1 : 1) catalyst dosage on the catalytic conversion performance of CO_2, different dosages of In-Zr (1 : 1) catalyst were placed in the DBD reactor using the IPC method, and the flow rate of CO_2 gas inlet was controlled at 20 mL min^{-1}, while the tests were carried out at different SIEs, and the results of the experiments are shown in Fig. 3a–d. Fig. 3a–c show the CO_2 conversion, CO yield and energy efficiency at different In-Zr (1 : 1) dosages, respectively. At low SIE, the CO_2 conversion, CO yield and energy efficiency of the catalyst-filled DBD are higher than those of the catalyst-free DBD due to the synergistic effect between the catalyst and the plasma, which promotes the conversion of CO_2. However, the CO_2 conversion of the DBD reactors filled with 0.3 g and 0.4 g of In-Zr (1 : 1) was ultimately lower than that of the catalyst-free DBD reactor at high SIE. This is due to the stacking of excess catalysts in the reactor, which makes it difficult for the catalyst to fully contact CO_2 and reduces its utilization rate, while a large amount of catalyst stacking hinders the plasma discharge, which ultimately leads to a decrease in the CO_2 conversion performance. Although the CO_2 conversion of 0.1 g In-Zr (1 : 1) at high SIE was slightly higher than that of empty DBD, its CO yield at high SIE was lower than that of empty DBD, which also matched with the lower CO selectivity of 0.1 g catalyst at high SIE (Fig. 3d). The possible reason for this situation is that the catalyst dosage is too low, and the catalysis is not sufficient. The overall trend of catalyst dosage is 0.2 g > 0.1 g > 0.3 g > 0.4 g. This indicates that excess catalysts tend to accumulate in the DBD reactor, which not only has a low utilization rate but also affects the plasma discharge, while insufficient dosage may lead to reduced catalytic activity. Therefore, the amount of catalyst needs to be strictly controlled.

The residence time of CO_2 gas in the DBD system influences its overall conversion efficiency. The residence time is determined using eqn (7), and the test results are illustrated in Fig. 3e and f. The CO_2 conversion rate rises with an increase in residence duration, irrespective of the presence of a catalyst (Fig. 3e). The duration of CO_2 gas presence in the discharge zone correlates positively with the likelihood of it being struck by energetic electrons. The CO_2 conversion in the In-Zr (1 : 1) system exceeds that of the DBD reactor without catalyst at extended residence times, whereas the CO_2 conversion in the catalyst-free DBD exceeds that of the catalyst-filled DBD at shorter residence times. This is likely because the catalyst needs

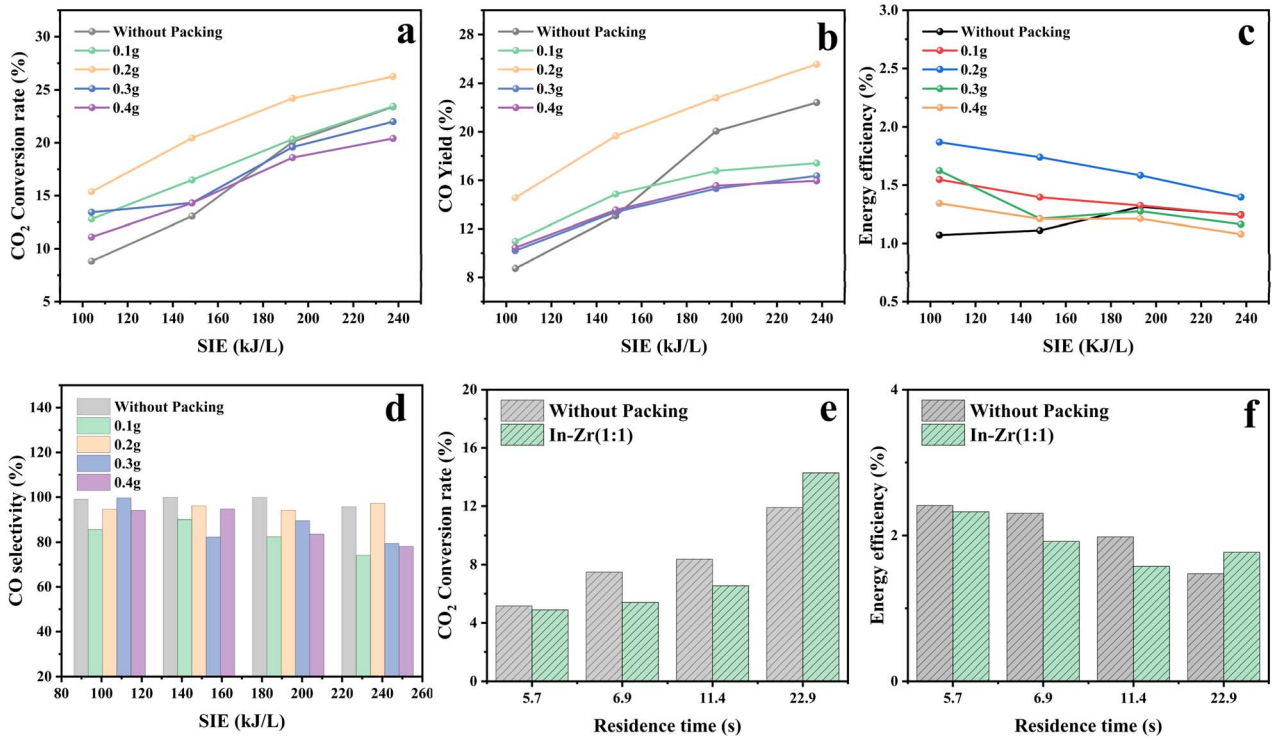

Fig. 3 The effect of SIE with different catalyst dosages on (a) CO_2 conversion rate, (b) CO yield, (c) energy efficiency, and (d) CO selectivity; the impact of residence time on (e) CO_2 conversion rate and (f) energy efficiency.

sufficient time to absorb CO_2; an inadequate residence time hinders CO_2 from adhering to the catalyst's surface, thus limiting its catalytic effect. The catalyst may also influence plasma discharge, resulting in reduced CO_2 conversion. Fig. 3f illustrates the correlation between energy efficiency and varying residence times, revealing a declining trend in energy efficiency as residence time increases. This phenomenon occurs because prolonged CO_2 presence in the system facilitates its heating by high-energy electrons. A greater amount of energy is expended as heat, leading to reduced energy efficiency. The energy efficiency of the reactor containing In-Zr (1 : 1) was significantly enhanced at the longest residence time of 22.9 seconds, suggesting that CO_2 and In-Zr (1 : 1) achieved optimal contact during this duration, allowing high-energy electrons to facilitate CO_2 conversion rather than dissipating energy as heat.

3.4 Mechanistic analysis

To examine the catalytic mechanisms of the catalysts In_2O_3, ZrO_2, In-Zr (1 : 1), and In-Zr (1 : 1)-DBD (the latter being derived from In-Zr (1 : 1) catalysts treated for 20 minutes in a DBD reactor under an air atmosphere at 160 V), XRD, XPS, EPR, and BET characterization tests were conducted. The findings are illustrated in Fig. 4. Fig. 4a presents the XRD diffractograms of several catalysts, demonstrating that the In_2O_3 and ZrO_2 samples align well with their respective PDF cards. In the In-Zr (1 : 1) composition, the typical peaks of the ZrO_2 sample are largely aligned, and the distinctive peaks of the In_2O_3 (211) crystal plane emerge at a 2θ diffraction angle of 21.5°.[38] This demonstrates that the In-Zr (1 : 1) composite catalyst was effectively synthesized. In contrast, the comparison of the In-Zr (1 : 1) catalysts prior to and following DBD treatment did not provide a discernible change, thus confirming that the DBD treatment does not influence the crystallinity of the catalysts.

Fig. 4b–g presents the XPS test results for several catalysts. Fig. 4b and c present the characterization test results for In 3d and Zr 3d, respectively. Notably, binding energies of 452.4 eV and 444.8 eV correspond to $In3d_{3/2}$ and $In3d_{5/2}$, while binding energies of 183.5 eV and 181.1 eV correspond to $Zr3d_{3/2}$ and $Zr3d_{5/2}$. This observation is attributed to the characteristic spin–orbit splitting of In^{3+} and Zr^{4+} ions. Comparing In_2O_3 and ZrO_2, both $In3d_{3/2}$ and $In3d_{5/2}$ in In-Zr (1 : 1) catalysts shift to lower binding energies, whereas $Zr3d_{3/2}$ and $Zr3d_{5/2}$ shift to higher binding energies. This indicates an electron transfer from Zr^{4+} to In^{3+} during the formation of In-Zr (1 : 1) catalysts.[39] This indicates that the In-Zr composite catalyst is not a simple physical mixture, but rather that chemical interactions occur between In_2O_3 and ZrO_2. To verify that such interactions are conducive to enhancing its catalytic performance, a physically mixed In-Zr composite catalyst was prepared and subjected to a series of tests and characterizations, with the results presented in Fig. S5. As can be seen from the XRD and TEM patterns in Fig. S5, the physically mixed In-Zr composite catalyst was successfully synthesized. Meanwhile, in comparison with the physically mixed In-Zr composite catalyst, the chemically combined In-Zr composite catalyst exhibits more oxygen vacancies, stronger CO_2 catalytic conversion capability, and superior thermal stability. All the above research results

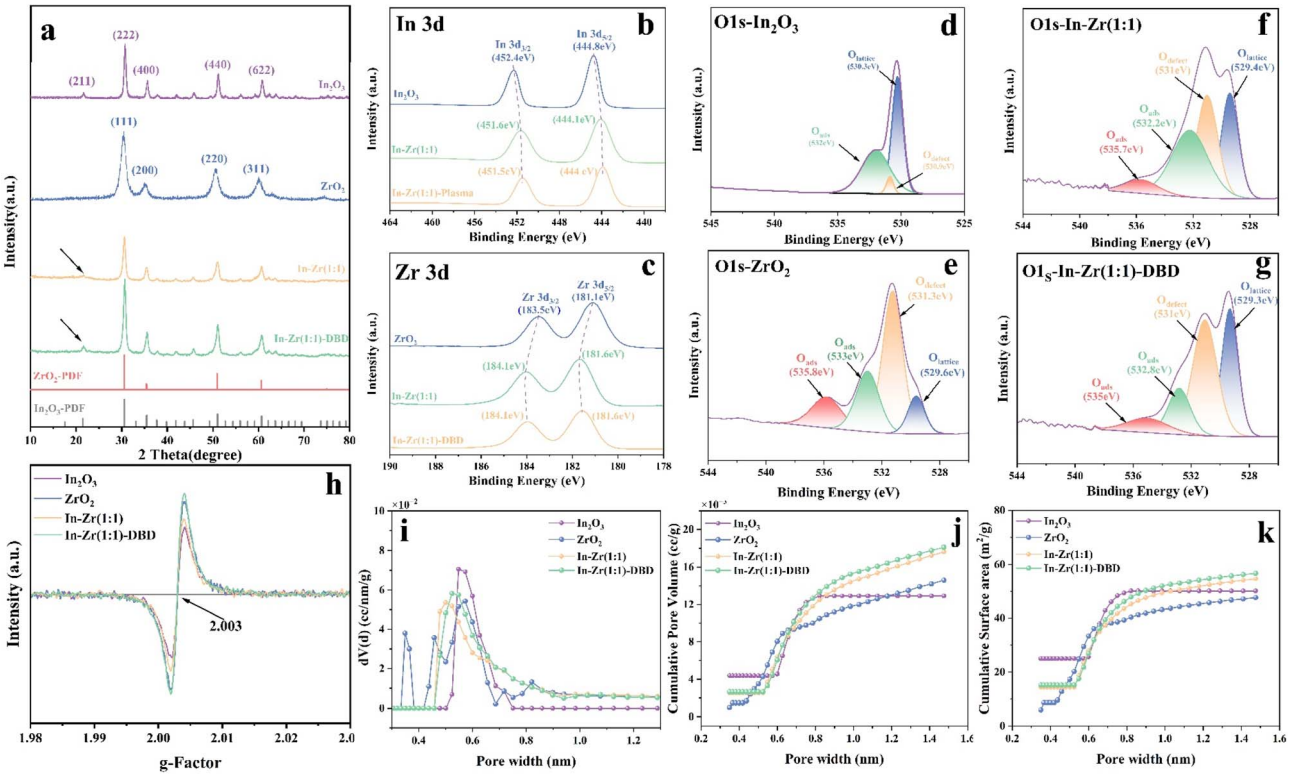

Fig. 4 (a) XRD patterns; XPS patterns of (b) In 3d, (c) Zr 3d, (d) O1s-In_2O_3, (e) O1s-ZrO_2, (f) O1s-In-Zr (1 : 1), and (g) O1s-In-Zr (1 : 1)-DBD; (h) EPR patterns of different catalysts; BET patterns of different catalysts with respect to (i) pore size distribution, (j) accumulated empty volume, and (k) cumulative surface area.

confirm that the interactions between In_2O_3 and ZrO_2 in the In-Zr composite catalyst have improved its catalytic conversion performance. In Fig. 4b and c, comparing In-Zr (1 : 1) with In-Zr (1 : 1)-DBD reveals no significant alteration in the binding energy of either In^{3+} or Zr^{4+}, indicating that the DBD treatment during catalyst synthesis does not influence the electronic states of In and Zr species.

Fig. 4d–g shows the O 1s spectra of the catalysts, indicating that oxygen exists in three forms for each catalyst. The species with a binding energy of around 530 eV corresponds to lattice oxygen (Olattice), the peak near 531 eV is attributed to surface oxygen vacancies (SOV), and the peak exceeding 532 eV is associated with the adsorbed oxygen (Oads)[40] on the catalyst surface. ZrO_2 exhibits a greater number of oxygen defects than In_2O_3, indicating its enhanced propensity for oxygen vacancy formation. The proportion of oxygen defects in the In-Zr (1 : 1) composition is lower than that in ZrO_2 but significantly higher than in In_2O_3, suggesting that the incorporation of ZrO_2 promotes the development of oxygen vacancies in the catalyst. Comparing the catalysts pre- and post-DBD treatment, the fraction of O-defects is significantly increased, indicating that DBD treatment promotes the creation of oxygen vacancies in the catalysts. XPS primarily indicates the existence of surface oxygen vacancies; hence, the formation of bulk oxygen vacancies (BOV) resulting from the migration of oxygen vacancies to the interior is not detectable in the XPS spectra.[41] To examine the potential migration of surface oxygen vacancies inside the catalysts, electron paramagnetic resonance spectroscopy (EPR) was employed for analysis, with the findings presented in Fig. 4h. The results indicate that both catalyst types exhibit distinctive signals associated with bulk oxygen vacancies at $g = 2.003$.[42] Table 2 presents the quantitative data on oxygen vacancies, illustrating the general findings. The order of oxygen vacancy concentration is In-Zr (1 : 1)-DBD > ZrO_2 > In-Zr (1 : 1) > In_2O_3, with the highest concentration of oxygen vacancies, 1.69×10^{13}, seen in the In-Zr (1 : 1)-DBD catalysts. This may result from the DBD treatment, where high-energy electrons produced by the plasma impact the catalyst,[41,43] leading to the removal of oxygen from its surface to create oxygen vacancies, while some surface oxygen vacancies migrate inward to form bulk oxygen vacancies. The presence of oxygen vacancies significantly enhances the catalytic conversion of CO_2,[44] elucidating the high efficiency of the In-Zr (1 : 1)-DBD catalysts in this process. In addition, the overall performance of DBD-assisted catalysis is excellent.[28]

Fig. 4i–k illustrate the pore size distribution, cumulative pore volume, and specific surface area plots of several catalysts, respectively. Fig. 4i illustrates the pore size distribution of several catalysts. Additionally, in combination with Table 2, it is observed that the average pore size of In_2O_3 is around 0.627 nm, while both ZrO_2 and In-Zr (1 : 1) exhibit an average pore size of 0.573 nm, and In-Zr (1 : 1)-DBD has an average pore size of 0.6 nm. All catalysts possess pore diameters in the microporous range, exceeding the kinetic diameter of the CO_2 molecule (0.48

Table 2 Bulk oxygen vacancies and surface adsorption data of catalysts

	BOV (spins per g)	Average pore width (nm)	Pore volume ($cm^3\ g^{-1}$)	Surface area ($m^2\ g^{-1}$)	CO_2 adsorption ($cm^3\ g^{-1}$)	E_g (eV)
In_2O_3	1.254×10^{13}	0.627	0.0129	50.154	5.68	2.7
ZrO_2	1.612×10^{13}	0.573	0.0144	47.716	4.57	4.58
In-Zr (1 : 1)	1.289×10^{13}	0.573	0.0176	54.694	5.54	2.58
In-Zr (1 : 1)-DBD	1.69×10^{13}	0.6	0.0181	56.689	5.86	2.49

nm), hence confirming their capacity to collect CO_2. While smaller pore sizes are unfavorable for CO_2 adsorption, excessively large pore sizes lead to the desorption of CO_2, making it easily dislodged. Therefore, In-Zr (1 : 1)-DBD, characterized by moderate pore sizes, is most conducive to CO_2 adsorption, corroborating the data presented in Table 2 and Fig. S6. Fig. 4j and k illustrate the cumulative pore volume and specific surface area plots of various catalysts, respectively. When considered alongside Table 2, it is evident that both the pore volume and surface area of the composite catalysts exceed those of the pure catalysts. This enhancement can be ascribed to the heterogeneous structure of the composite catalysts, which induces surface defects, thereby augmenting pore volume and specific surface area.[45] The In-Zr (1 : 1)-DBD catalyst exhibited the greatest pore volume of 0.181 $cm^3\ g^{-1}$ and the highest specific surface area of 56.689 $m^2\ g^{-1}$. This is likely due to a substantial quantity of high-energy electrons produced by the DBD impacting the catalyst surface, resulting in an increased number of defects on the catalyst surface. The combination of elevated pore volume and increased specific surface area enhances CO_2 capture by the catalysts, elucidating why the peak CO_2 adsorption (5.86 $cm^3\ g^{-1}$) in Table 2 and Fig. S6 is seen in In-Zr (1 : 1)-DBD. Meanwhile, in Fig. S6, the incomplete closure of the desorption curve indicates strong adsorption of CO_2 by the catalyst under the tested conditions, correlating with its excellent adsorption performance.

Both In_2O_3 and ZrO_2 are classified as semiconductor materials. The forbidden bandwidth (E_g) is a critical performance metric for semiconductors. To investigate the E_g of various catalysts, UV reflectance spectra were transformed over the range of 200–800 nm to establish the correlation between $(\alpha h\nu)^2$ and the optical energy ($h\nu$). The bandgap value was determined from the intersection of the tangent line with the horizontal axis,[46] with results presented in Fig. S7 and Table 2. The bandgap of In_2O_3 is 2.7 eV, that of ZrO_2 is 4.58 eV, and that of the composite catalyst In-Zr (1 : 1) is 2.58 eV. The likely cause of this scenario is that the composite material has a greater number of defects (*e.g.*, oxygen vacancies), which possess energy levels that reduce the energy gap between the valence and conduction bands. Conversely, In-Zr (1 : 1)-DBD exhibits the lowest band gap, $E_g = 2.49$ eV, indicating that the bombardment of the catalyst by high-energy electrons produced by the plasma has induced a greater number of defects within the catalyst. This facilitates electron transitions from the valence band to the conduction band, thereby augmenting the catalyst's electrical conductivity.[47] The reduced band gap further implies an increased susceptibility to excitation by the plasma, both of which enhance the catalyst's efficacy in CO_2 reduction.

3.5 Density functional theory (DFT) simulations

To further elucidate the underlying mechanism, DFT simulations were conducted using the VASP program. Based on the XRD analysis results, the oxygen vacancy formation energies and CO_2 adsorption energies corresponding to the crystal planes of the strongest peaks and second-strongest peaks of In_2O_3, ZrO_2, and In-Zr (1 : 1) were calculated. Meanwhile, the structural schematics of CO_2 adsorption on different crystal planes were simulated, charge distribution of CO_2 adsorbed on the heterojunction surface of In-Zr composite catalysts with and without oxygen vacancies, as shown in Fig. 5, and the specific calculation results are presented in Table 3. The equations used to calculate the oxygen vacancy formation energy (E_{vac}), the CO_2 adsorption energy (E_{ads}) and the charge density ($\Delta\rho$) were as follows.

$$E_{vac} = E_D + 1/2E_{O_2} - E_P \quad (8)$$

$$E_{ads} = E_{(slab\text{-}CO_2)} - E_{slab} - E_{CO_2} \quad (9)$$

$$\Delta\rho = \rho_{total} - \rho_{substrate} - \rho_{adsorbate} \quad (10)$$

According to the data in Table 3, it can be seen that E_{vac} follows the trend of ZrO_2 < In-Zr (1 : 1) < In_2O_3. In general, smaller oxygen vacancy formation energy indicates that it is easier to form oxygen vacancies,[48] from which it can be inferred that the oxygen vacancy content roughly follows the trend of ZrO_2 > In-Zr (1 : 1) > In_2O_3. In addition, the E_{ads} was −2.749 eV at the ZrO_2 end face and −2.383 eV at the In_2O_3 end face, which were much smaller than those of the pure In_2O_3 and ZrO_2, suggesting that compared to the In_2O_3 and ZrO_2, the composite In-Zr (1 : 1) catalyst was more favorable for the thermodynamics of the CO_2 adsorption.[49] In-Zr (1 : 1) not only exhibits a lower oxygen vacancy formation energy but also has the lowest CO_2 adsorption energy. Although the actual formation of oxygen vacancy and CO_2 adsorption is influenced by external kinetic factors and sample morphology, these results still explain the excellent CO_2 catalytic conversion performance of In-Zr (1 : 1) composite catalysts.

The differential charge density distributions clearly show distinct charge-transfer behaviors for the two systems. On the pristine In_2O_3-ZrO_2 surface (Fig. 5), only limited electron accumulation is observed around the adsorbed CO_2 molecule, corresponding to a small electron transfer of $0.171|e|$. In contrast, the introduction of an oxygen vacancy leads to a much stronger electronic interaction between CO_2 and the catalyst surface (Fig. 5), resulting in a substantial electron transfer of $0.875|e|$.

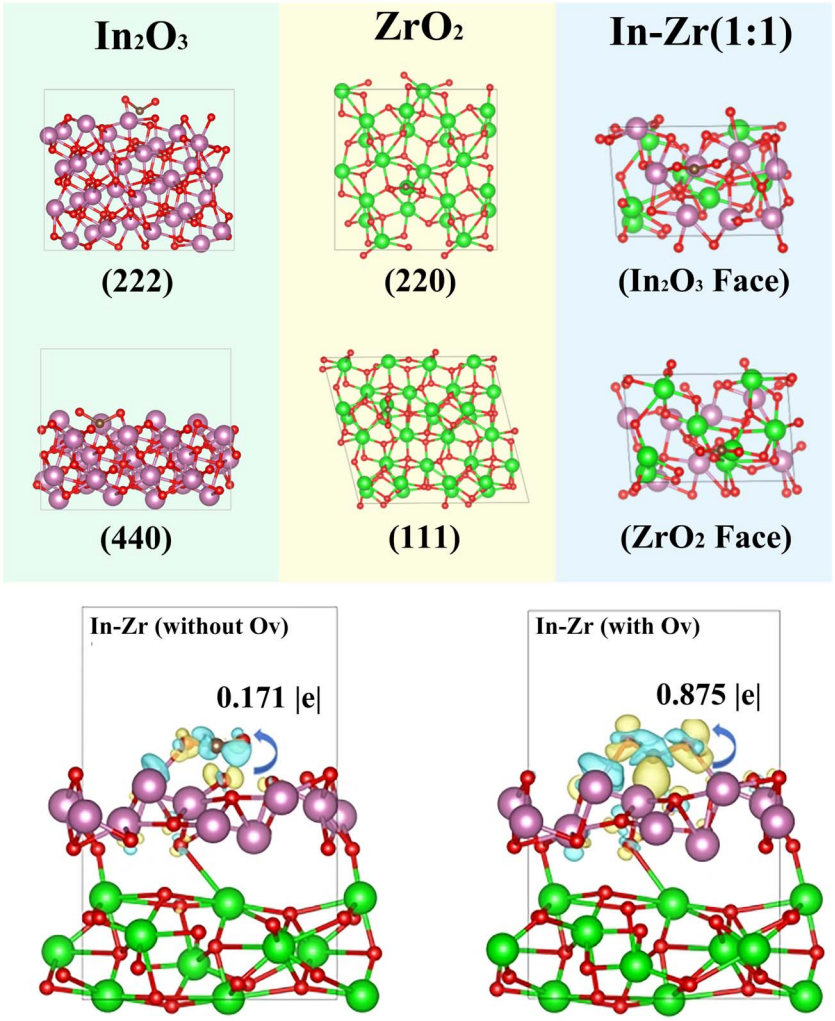

Fig. 5 Schematic structure of CO_2 adsorption on different crystalline surfaces of In_2O_3, ZrO_2 and In-Zr (1 : 1).

Table 3 Calculated data on the correlation energies of different crystal faces of In_2O_3, ZrO_2 and In-Zr (1 : 1)

	In_2O_3 (222)	In_2O_3 (440)\	ZrO_2 (220)	ZrO_2 (111)	In-Zr (1 : 1) In_2O_3 face	In-Zr (1 : 1) ZrO_2 face
E_{O_2}	−9.893					
E_{CO_2}	−22.95					
E_D	−841.839	−425.727	−651.834	−8783787	−298.191	−297.414
E_P	−849.335	−433.285	656.006	−883.475	−303.285	−304.541
$E_{CO_2\text{-slab}}$	−866.13	−450.104	−676.709	−903.519	−323.524	−323.113
E_{vac}	2.549	2.611	−0.774	−0.259	0.148	2.181
E_{ads}	−1.341	−1.427	−1.925	−1.782	−2.383	−2.749

This pronounced charge enrichment on the defective surface indicates that the oxygen vacancy greatly enhances the electron donation ability of the catalyst, thereby strengthening the activation of the adsorbed CO_2. The results demonstrate that oxygen vacancies play a critical role in strengthening electron donation to CO_2, thereby boosting its activation and improving the overall catalytic performance of the In_2O_3-ZrO_2 heterojunction.

3.6 Evaluation of catalytic efficiency

Fig. 6 illustrates a comparison between the present study and previous studies conducted over the past five years, demonstrating that the In-Zr (1 : 1) catalyst developed herein achieves the highest CO_2 conversion rate at moderate input power. The catalyst formulated in this work shows a distinct advantage, underscoring its potential for future applications.

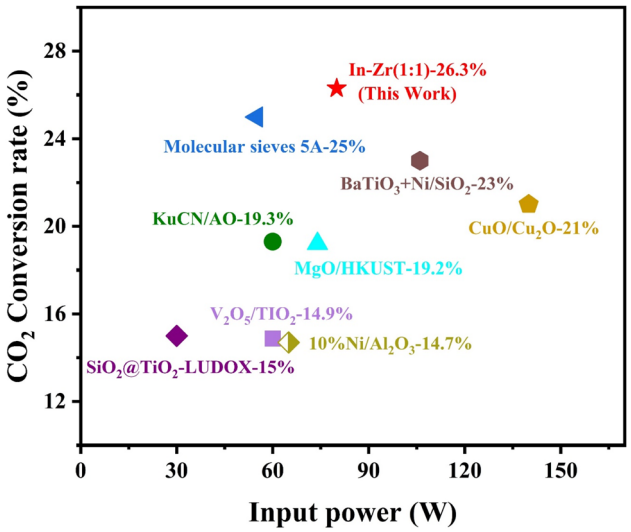

Fig. 6 Benchmarking of catalytic CO_2 conversion performance: current study *vs.* state-of-the-art systems (2019–2023).[26,29,50–55]

This work presents a schematic mechanism for the improved conversion of CO_2 using In-Zr composite catalysts inside the DBD reaction system, integrating experimental characterization and DFT simulations (Fig. 7). Plasma catalysis can generate both homogeneous and heterogeneous reactions.[56] In the catalyst-free DBD reactor, the predominant homogeneous reaction involves high-energy electrons dissociating CO_2 molecules *via* electron impact, which is the principal route for CO_2 dissociation in the DBD plasma reactor. Upon introducing the catalyst into the DBD reactor, both homogeneous reactions in the gas phase and heterogeneous reactions on the catalyst occur simultaneously,[54] and this interplay enhances the overall CO_2 conversion efficiency of the system. Furthermore, introducing an In-Zr composite catalyst into the discharge zone of the DBD reactor facilitates the emergence of novel CO_2 decomposition reaction pathways, supplementing the existing high-energy electron excitation mechanism. There are primarily three pathways to enhance the CO_2 conversion efficiency of the system. (1) A significant quantity of oxygen vacancies, as demonstrated in our prior research and existing literature, can significantly facilitate the conversion of CO_2 in the DBD reactor. Oxygen vacancies on the catalyst will sequester CO_2 gas molecules within the reactor, extending their residence time in the discharge zone, thereby increasing their likelihood of collision with high-energy electrons and eventually improving the total catalytic conversion efficiency.[57] (2) The BET analysis indicates that the In-Zr composite catalyst possesses the highest specific surface area and the greatest pore volume. A larger specific surface area facilitates enhanced interaction between CO_2 gas molecules and the catalyst, while an increased pore volume allows for greater adsorption of CO_2 gas molecules by the catalyst. (3) Upon plasma activation, the reduced bandgap promotes the separation of electron–hole pairs inside the catalyst, allowing electrons to be transported to the adsorbed CO_2 molecules on the catalyst's surface, thereby facilitating the breakdown of CO_2. The reduced bandgap facilitates the separation of hole–electron pairs while impeding their recombination, which greatly benefits the catalytic conversion of CO_2. Moreover, introducing a catalyst into the DBD reactor alters the plasma discharge from filamentary to a hybrid filamentary-surface mode. This modification augments the electric field

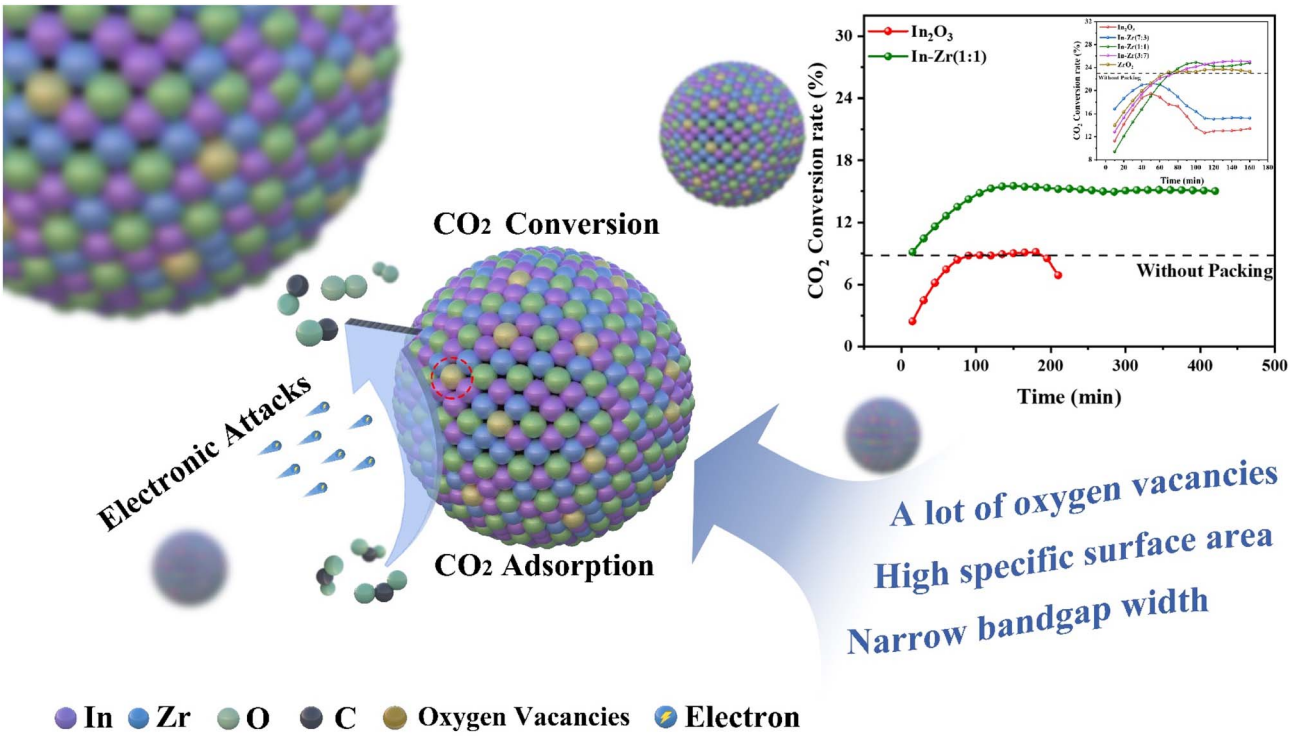

Fig. 7 Mechanistic analysis of the superior comprehensive catalytic performance in In-Zr composite catalysts.

strength in the discharge region, thereby stabilizing the discharge and enhancing CO_2 conversion.

4. Conclusion

In summary, a series of In_2O_3-ZrO_2 composite catalysts were developed through co-precipitation and post-modified using DBD plasma for CO_2 decomposition in a plasma-catalytic system. The In-Zr (1 : 1) composition exhibited optimal performance, achieving a CO_2 conversion rate of 26.3% with CO selectivity exceeding 90%, along with excellent thermal stability and a prolonged catalytic lifetime of up to 450 minutes. Comprehensive characterization and DFT analysis confirmed that the superior performance originates from (i) the generation of abundant oxygen vacancies, (ii) enhanced specific surface area and pore volume, and (iii) a reduced bandgap promoting charge separation. These factors collectively improve CO_2 adsorption, activation, and electron transfer under plasma conditions. The results offer an engineering-oriented strategy for designing robust and efficient plasma-catalyst systems suitable for scalable CO_2 conversion applications.

Author contributions

Sai Li: conceptualization, methodology, investigation, writing – original draft. Yuhang Wang: data curation, validation, writing – original draft. Kui Zhang: conceptualization, methodology. Shaobo Jia: writing – review & editing. Dongyuan Yang: conceptualization, supervision. Peng Ren: writing – review & editing. Zekai Ma: methodology. Shuoshuo Wang: methodology, validation. Haixia Wu: data curation. Yameng Ma: supervision. Qi Chen: methodology. Jiahao Zhouhuang: investigation. Qiuliang Yu: investigation. Lihui Zeng: validation. Rui Tan: writing – review & editing. Zhiming Feng: methodology, supervision, writing – review & editing. Qing Feng: supervision, writing – review & editing.

Conflicts of interest

The authors declare that they have no known competing financial interests or personal relationships that could have appeared to influence the work reported in this paper.

Data availability

All data included in this article are available upon request by contacting the corresponding author.

Supplementary information (SI) is available. See DOI: https://doi.org/10.1039/d5ta08108d.

Acknowledgements

This work was financially supported by the Natural Science Foundation of China (NSFC, No. 22109126), Shaanxi Province key research and development plan item (2024CY2-GJHX-72), Yulin City science and technology plan project (2023-CXY-189), Key Laboratory of Coal Resources Exploration and Comprehensive Utilization, Ministry of Land Resources (SMDZ-KF2024-3), and Shaanxi Province Key Point Research and Development Project (2022GY-378).

References

1 T. P. Hughes, J. T. Kerry, A. H. Baird, S. R. Connolly, T. J. Chase, A. Dietzel, T. Hill, A. S. Hoey, M. O. Hoogenboom, M. Jacobson, A. Kerswell, J. S. Madin, A. Mieog, A. S. Paley, M. S. Pratchett, G. Torda and R. M. Woods, *Nature*, 2019, **568**, 387–390.
2 D. Li, J. Liu, X. Chen, Z. Feng, S. Wang, Y. Wang, N. Lin, J. Wu and Y. Feng, *Appl. Catal., B*, 2024, **365**, 124824.
3 S. Z. Xingpeng Tian, H. Hongqing, R. R. Gaddam, R. C. Dutta, H. Wang, B. Wu, N. P. Brandon and R. Tan, *Chain*, 2025, **2**, 38–54.
4 D. Li, S. Xie, J. Liang, B. Ma, J. Fu, J. Wu, Y. Feng and Z. Feng, *Sep. Purif. Technol.*, 2024, **340**, 126545.
5 Z. Feng, G. Gupta and M. Mamlouk, *Int. J. Hydrogen Energy*, 2023, **48**, 25830–25858.
6 Y. Luo, Y. Qiao, H. He, M. Chen, G. Liu, X. Liu, L. Pan, Z. Feng and R. Tan, *J. Power Sources*, 2025, **631**, 236297.
7 S. Li, Z. Xin, J. Han, Z. Feng, G. Liao, S. Wang, K. Liu, Q. Li, T. X. Liu and M. Bayati, *Ionics*, 2024, **30**, 7213–7222.
8 Z. Feng, S. Zheng, H. Che and Z. Gao, *J. Alloys Compd.*, 2025, **1044**, 184360.
9 S. C. Roy, O. K. Varghese, M. Paulose and C. A. Grimes, *ACS Nano*, 2010, **4**, 1259–1278.
10 R. M. Cuéllar-Franca and A. Azapagic, *J. CO2 Util.*, 2015, **9**, 82–102.
11 Z. Zhang, T. Wang, M. J. Blunt, E. J. Anthony, A.-H. A. Park, R. W. Hughes, P. A. Webley and J. Yan, *Appl. Energy*, 2020, **278**, 115627.
12 S. Ian, G. Andrey, A. D. Ibadillah, L. Xueqian, A. A. Harry, A. V. David and X. Chengxiang, *Nat. Catal.*, 2021, **4**, 952–958.
13 Y. Zhao, R. Tan, J. Yang, K. Wang, R. Gao, D. Liu, Y. Liu, J. Yang and F. Pan, *J. Power Sources*, 2017, **340**, 160–166.
14 A. H. Khoja, M. Tahir and N. A. S. Amin, *Energy Convers. Manage.*, 2019, **183**, 529–560.
15 A. George, B. Shen, M. Craven, Y. Wang, D. Kang, C. Wu and X. Tu, *Renewable Sustainable Energy Rev.*, 2020, **135**, 109702.
16 S. Li, M. Ongis, G. Manzolini and F. Gallucci, *Chem. Eng. J.*, 2021, **410**, 128335.
17 J. Liu, S. Xie, D. Li, Z. Feng, H. Lu, X. Li, J. Liang, B. Ma, J. Fu, J. Xie, X. Zhi and Y. Feng, *Appl. Catal., B*, 2025, **379**, 125700.
18 M. F. Mustafa, X. Fu, Y. Liu, Y. Abbas, H. Wang and W. Lu, *J. Hazard. Mater.*, 2018, **347**, 317–324.
19 M. Alliati, D. Mei and X. Tu, *J. CO2 Util.*, 2018, **27**, 308–319.
20 V. Maslova, R. Nastase, G. Veryasov, N. Nesterenko, E. Fourré and C. Batiot-Dupeyrat, *Prog. Energy Combust. Sci.*, 2024, **101**, 101096.
21 V. Damideh, O. H. Chin, H. A. Gabbar, S. J. Ch'ng and C. Y. Tan, *Vacuum*, 2020, **177**, 109370.
22 H. Guo, Z. Li, Y. Zhang, N. Jiang, H. Wang and J. Li, *Sep. Purif. Technol.*, 2020, **253**, 117540.
23 Y. Wang, Z. Liao, S. Mathieu, F. Bin and X. Tu, *J. Hazard. Mater.*, 2021, **404**, 123965.

24 L. Wang, Y. Yi, H. Guo and X. Tu, *ACS Catal.*, 2017, **8**, 90–100.
25 A. H. Babikir, M. G. M. Ekanayake, O. Oloye, J. D. Riches, K. Ostrikov and A. P. O'Mullane, *Adv. Funct. Mater.*, 2023, **34**, 117540.
26 N. Lu, N. Liu, C. Zhang, Y. Su, K. Shang, N. Jiang, J. Li and Y. Wu, *Chem. Eng. J.*, 2021, **417**, 129283.
27 D. Ray, P. Chawdhury and C. Subrahmanyam, *Environ. Res.*, 2020, **183**, 109286.
28 M. Umamaheswara Rao, K. Bhargavi, G. Madras and C. Subrahmanyam, *Chem. Eng. J.*, 2023, **468**, 143671.
29 H. Hadi, K. Mohammadreza and S. Babak, *Results Eng.*, 2024, **24**, 102884.
30 Y.-X. Pan, Y. You, S. Xin, Y. Li, G. Fu, Z. Cui, Y.-L. Men, F.-F. Cao, S.-H. Yu and J. B. Goodenough, *J. Am. Chem. Soc.*, 2017, **139**, 4123–4129.
31 D. Cai, Y. Cai, K. B. Tan and G. Zhan, *Materials*, 2023, **16**, 2803.
32 S. Li, Y. Wang, K. Zhang, H. Zhu, G. Liao, Q. Li, S. Jia, Q. Feng, J. Pan, R. Tan, Z. Feng and D. Yang, *J. Alloys Compd.*, 2025, 183304, DOI: 10.1016/j.jallcom.2025.183304.
33 Q. Li, G. Liao, N. Liu, Z. Feng, H. Zhu, S. Jia, Y. Wang, Z. Ma, K. Zhang, Q. Feng, D. Yang and S. Li, *J. Phys. D: Appl. Phys.*, 2025, **58**, 375205.
34 G. Liao, S. Li, Y. Luo, Z. Xin, Q. Li, R. Tan, K. Zhang and Z. Feng, *J. Alloys Compd.*, 2025, **1013**, 178599.
35 P. Chen, J. Shen, T. Ran, T. Yang and Y. Yin, *Plasma Sci. Technol.*, 2017, **19**, 125505.
36 D. H. Mei, S. Y. Liu and X. Tu, *J. CO2 Util.*, 2017, **21**, 314–326.
37 L. Na, Z. Chuke, S. Kefeng, J. Nan, L. Jie and W. Yan, *J. Phys. D: Appl. Phys.*, 2019, **52**, 224003.
38 M. N. Shabbir, R. Alabada, M. Aadil, Z. Ahmad, A. A. Alothman, N. A. Almuhous, W. A. Khan and R. M. K. Mohamed, *Ceram. Int.*, 2024, **50**, 4404–4414.
39 L. Wang, B. Cheng, L. Zhang and J. Yu, *Small*, 2021, **17**, 2103447.
40 A. Tsoukalou, P. M. Abdala, A. Armutlulu, E. Willinger, A. Fedorov and C. R. Müller, *ACS Catal.*, 2020, **10**, 10060–10067.
41 S. Li, G. Liao, D. Bildan, Z. Feng, H. Cai, J. Han, Z. Xin, K. Liu, Q. Li, J. Shang and T. X. Liu, *Int. J. Hydrogen Energy*, 2024, **67**, 448–457.
42 R. Bian, S. An, X. Wang, Y. Xue, J. Tian, Z. Liang and Z. Song, *Int. J. Hydrogen Energy*, 2024, **51**, 787–795.
43 X. Hu, J. Wang, J. Wang, Y. Deng, H. Zhang, T. Xu and W. Wang, *Appl. Catal., B*, 2022, **318**, 121879.
44 X. Liu, M. Wang, C. Zhou, W. Zhou, K. Cheng, J. Kang, Q. Zhang, W. Deng and Y. Wang, *Chem. Commun.*, 2018, **54**, 140–143.
45 X. Sun, J. Wu, F. Tian, W. Zhang and Q. Li, *Mater. Res. Bull.*, 2018, **103**, 247–258.
46 D. Triyono, U. Hanifah and H. Laysandra, *Results Phys.*, 2020, **16**, 102995.
47 T. Xiong, W. Cen, Y. Zhang and F. Dong, *ACS Catal.*, 2016, **6**, 2462–2472.
48 H. Zhu, X. Song, X. Han, X. Zhang, J. Bao, N. Zhang and G. He, *Environ. Sci. Technol.*, 2020, **54**, 8601–8611.
49 J. Li, X. Zhai, C. Ma, S. Zhu, F. Yu, B. Dai, G. Ge and D. Yang, *Nanomaterials*, 2019, **9**, 1595.
50 H. Hatami, M. Khani, S. A. Razavi Rad and B. Shokri, *Heliyon*, 2024, **10**, e26280.
51 P. Kaliyappan, A. Paulus, J. D'Haen, P. Samyn, Y. Uytdenhouwen, N. Hafezkhiabani, A. Bogaerts, V. Meynen, K. Elen, A. Hardy and M. K. Van Bael, *J. CO2 Util.*, 2021, **46**, 101468.
52 L. Xia, M. Wu, Y. Li, H. Guo, Y. Cheng and G. Meng, *Energy Fuels*, 2023, **38**, 565–575.
53 X. Ma, S. Li, M. Ronda-Lloret, R. Chaudhary, L. Lin, G. van Rooij, F. Gallucci, G. Rothenberg, N. Raveendran Shiju and V. Hessel, *Plasma Chem. Plasma Process.*, 2018, **39**, 109–124.
54 K. Zhang, G. Zhang, X. Liu, A. N. Phan and K. Luo, *Ind. Eng. Chem. Res.*, 2017, **56**, 3204–3216.
55 W. Taobo, L. Hongxia, X. Xiang and F. Xinxin, *IOP Conf. Ser. Earth Environ. Sci.*, 2017, **52**, 012100.
56 X. Fan, T. Zhu, Y. Sun and X. Yan, *J. Hazard. Mater.*, 2011, **196**, 380–385.
57 Y. Lu, X. Li, X. Jing, Y. Huang, Y. Qiang, G. Cao, R. Qin, Q. Cao, J. Cao and S. C. Lee, *Surf. Interfaces*, 2024, **53**, 104957.